Journal of Geophysical Research: Atmospheres

RESEARCH ARTICLE
10.1002/2017JD028106

Key Points:
- The relationship between presummer extreme rainfall in south China and synoptic disturbances in 1998–2015 is examined by a spectral analysis
- Major synoptic disturbances originate downstream of the Tibetan Plateau, accompanied by cold fronts or midlatitude Rossby wave trains
- The structures and evolution of the major synoptic disturbances are revealed using their composite anomalous fields

Correspondence to:
Y. Luo,
ylluo@cma.gov.cn

Citation:
Huang, L., Luo, Y., & Zhang, D.-L. (2018). The relationship between anomalous Presummer extreme rainfall over south China and synoptic disturbances. *Journal of Geophysical Research: Atmospheres*, *123*. https://doi.org/10.1002/2017JD028106

Received 23 NOV 2017
Accepted 6 MAR 2018
Accepted article online 10 MAR 2018

The Relationship Between Anomalous Presummer Extreme Rainfall Over South China and Synoptic Disturbances

Ling Huang[1], Yali Luo[1,2], and Da-Lin Zhang[1,3]

[1]State Key Laboratory of Severe Weather, Chinese Academy of Meteorological Sciences, Beijing, China, [2]Collaborative Innovation Center on Forecast and Evaluation of Meteorological Disasters, Nanjing University of Information Science and Technology, Nanjing, China, [3]Department of Atmospheric and Oceanic Science, University of Maryland, College Park, College Park, MD, USA

Abstract A spectral analysis of daily rainfall data has been performed to investigate extreme rainfall events in south China during the presummer rainy seasons between 1998 and 2015 (excluding 1999, 2006, 2011, and 2014). The results reveal a dominant frequency mode at the synoptic scale with pronounced positive rainfall anomalies. By analyzing the synoptic-scale bandpass-filtered anomalous circulations, 24 extreme rainfall episodes (defined as those with a daily rainfall amount in the top 5%) are categorized into "cyclone" (15) and "trough" (8) types, with the remaining events as an "anticyclone" type, according to the primary anomalous weather system contributing to each extreme rainfall episode. The 15 cyclone-type episodes are further separated into (11) lower- and (4) upper-tropospheric migratory anomalies. An analysis of their anomalous fields shows that both types could be traced back to the generation of cyclonic anomalies downstream of the Tibetan Plateau, except for two episodes of lower-tropospheric migratory anomalies originating over the South China Sea. However, a lower-tropospheric cyclonic anomaly appears during all phases in the former type, but only in the wettest phase in the latter type, with its peak disturbance occurring immediately beneath an upper-level warm anomaly. The production of extreme rainfall in the trough-type episodes is closely related to a deep trough anomaly extending from an intense cyclonic anomaly over north China, which in turn could be traced back to a midlatitude Rossby wave train passing by the Tibetan Plateau. The results have important implications for understanding the origin, structure, and evolution of synoptic disturbances associated with the presummer extreme rainfall in south China.

1. Introduction

The presummer rainy season (i.e., April–June) in south China is the first rainy season to occur during the early East Asian summer monsoon (Ding, 1994). This rainy season typically contributes approximately half of the annual precipitation amount. The maximum seasonal rainfall accumulation regularly exceeds 800 mm and is usually found in the central and coastal provinces of Guangdong (Luo et al., 2017). Such heavy rainfall events can result in catastrophic consequences such as extensive flooding and landslides, leading to considerable damage to human society and the natural environment. Hence, it is of vital importance to understand and accurately predict these heavy rainfall events in order to facilitate advanced societal planning, decision-making, and hazard mitigation.

Most of the heavy rainfall events in south China are produced by mesoscale convective systems (MCSs; Luo, Wang, et al., 2013; Xia et al., 2015). Numerous studies have examined the mechanisms of heavy rainfall production in MCSs and their associated favorable environmental conditions. Some major favorable conditions include quasi-stationary fronts (Chen, 1983), low-level vortices (Chang et al., 1998; Fu et al., 2010; Huang & Meng, 2014; Ninomiya & Akiyama, 1992; Tao & Ding, 1981), and low-level, southwesterly jets (Chen & Yu, 1988; Chen, Wang, & Lin, 2005, 2006; Huang & Luo, 2017; C. C. Wang, Hsu, et al., 2014). In addition, onshore oceanic flow, surface mesoscale outflow boundary, frictional contrast between land and sea, and coastal orography could all play critical roles in the initiation and development of heavy-rain-producing MCSs in the coastal areas of south China (H. Wang, Luo, et al., 2014; Wu & Luo, 2016). Nevertheless, it appears to be that the larger-scale disturbances, in which the heavy-rain-producing MCSs are embedded, preferentially determine whether or not heavy rainfall episodes will occur given the favorable lifting conditions for convection (e.g., Doswell et al., 1996; Johns & Doswell, 1992).

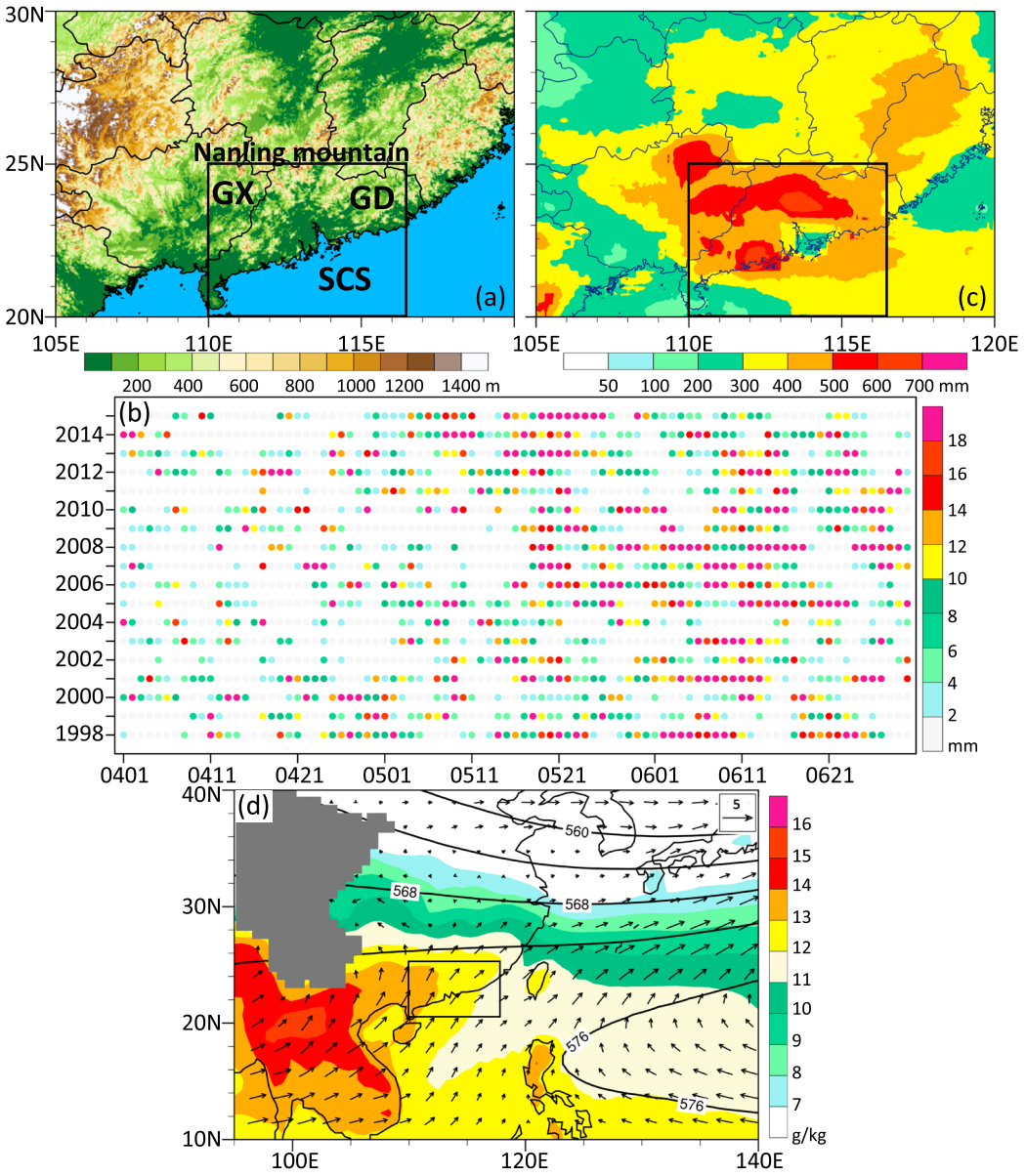

Figure 1. (a) Terrain over south China and its adjacent area. (c) Accumulated precipitation (mm) during 1 May to 15 June averaged between 1998 and 2015 using the CMORPH data set. (b) Domain-averaged daily rainfall from 1 April to 30 June during 1998–2015. (d) Specific humidity (shadings; g kg^{-1}) and wind field (m s^{-1}) at 850 hPa, and the geopotential height (10 gpm, black contour) at 500 hPa, averaged from 1 May to 15 June between 1998 and 2015 using the ERA-Interim data. An inner box in (a), (c), and (d) indicates the key region of the present study, which is used similarly in the rest of the figures. Symbols "GX," "GD," and "SCS" in (a) indicate the provinces of Guangxi and Guangdong and the South China Sea, respectively.

Numerous studies have examined the impact of synoptic-scale disturbances and the intraseasonal oscillation (ISO) on heavy rainfall production using the temporal filtering technique (e.g., Li & Zhou, 2015; Liu et al., 2014). The ISO modes influencing heavy rainfall events over south China during the presummer rainy season have not received much attention until recently (Chen, Wei, & Xiu, 2014; Hong & Ren, 2013; Li & Zhou, 2015; Pan et al., 2013), when compared with the large volume of literature concerning the ISO impact over the Yangtze and Huai River basins in eastern China during midsummer (X. Zhang, Guo, & He, 2002; Q. Zhang, Tao, & Zhang, 2003; Zhu et al., 2003; Yang & Li, 2003; Mao & Wu, 2006; Mao, Zhang, & Wu, 2010; Yang et al., 2010, 2013; Chen & Zhai, 2014; Liu, Zhang, & Wang, 2008, Liu et al., 2014; Sun et al., 2016). Previous studies have found the importance of subseasonal sea surface temperature anomalies (Hong & Ren, 2013), the

Madden-Julian Oscillation (MJO; Chen et al., 2014), the biweekly oscillation (Pan et al., 2013), and interactions between synoptic disturbances and ISOs (Li & Zhou, 2015) in heavy rainfall production in south China. These studies are conducted by compositing all the anomalies based on the phases of the disturbances concerned, regardless of the different types of anomalies or mechanisms that may modulate individual heavy rainfall events. The composite fields obtained tend to smooth out some distinct features that might be categorized into various groups.

While ISOs could provide a favorable background for continuous moisture supply and quasi-geostrophic forcing, traveling synoptic-scale disturbances, known as the succession of synoptic-scale (3–8 day) disturbances in the atmospheric circulation (Berry et al., 2012), are often associated with individual heavy rainfall events in, for example, the Yangtze and Huai river basins (Jiao et al., 2004; Qian et al., 2004; Zhang & Zhang, 2012), the intertropical convergence zone (Gu & Zhang, 2001), the equator region (Chang, Harr, & Chen, 2005), the western Pacific (Tam & Li, 2006), and the Australian monsoon region (Berry et al., 2012). However, little is known about the statistical characteristics of synoptic disturbances causing presummer heavy rainfall over south China, given their importance in heavy rainfall production in the above mentioned regions. Therefore, conducting a systematic investigation of the synoptic-scale disturbances in association with a large number of presummer heavy rainfall episodes in south China, including their spatial characteristics and tracks of movements, is highly desirable.

In view of the lack of knowledge of the relationship between synoptic disturbances and extreme rainfall production in south China, we will attempt to answer the following questions through the present study: What are the origin, structures and evolution of synoptic-scale disturbances associated with extreme rainfall episodes in south China during the presummer rainy season? How do they interact with other favorable features in the extreme rainfall production over this region? These questions will be addressed by applying spectral analysis and filtering algorithms to the rainfall and reanalysis data sets of 1998–2015.

The next section introduces the data, spectral analysis, and filtering methodology used in this study. Section 3 describes the spatiotemporal characteristics of daily rainfall anomalies and the classification of bandpass-filtered circulation patterns associated with the extreme rainfall episodes. Section 4 presents analyses of the composite filtered circulations in the lower and upper troposphere that are associated with each classified type of extreme rainfall episodes. A summary and some concluding remarks are given in the final section.

2. Data and Methodology

2.1. Data Description

The new version of the high-resolution global precipitation data sets from the National Oceanic and Atmospheric Administration Climate Prediction Center MORPHing technique (CMORPH; Joyce et al., 2004) has been used to estimate daily rainfall in this study. This version of the CMORPH has a spatial resolution of 8 km and 30 min intervals between 60°N and 60°S and covers the entire Tropical Rainfall Measuring Mission (Kummerow et al., 1998) era from January 1998 to 2015, with the bias correction and rain gauge-satellite data blended in with the raw, satellite only precipitation estimates. Previous studies have shown not only the reliability of the CMORPH data set on diurnal cycle, daily rainfall, warm season, and annual rainfall estimation (Fitzjarrald et al., 2008; Hirpa et al., 2010; Luo, Qian, et al., 2013; Pereira Filho et al., 2010; Shen et al., 2010) but also the reliability of the spatial pattern and temporal variations of precipitation using Chinese rain gauge reports from ~2000 stations (Shen et al., 2010). Besides, the CMORPH data set includes the needed rainfall information over the South China Sea (SCS) that is not available from the conventional surface-based observations. The daily rainfall rates to be used for spectral analysis are calculated from 00 UTC to 00 UTC on the next day.

The Interim European Centre for Medium-Range Weather Forecasts reanalysis (ERA-Interim; Dee et al., 2011) with a 0.75° spatial resolution and 6 h time intervals is used herein to depict the large-scale circulation patterns associated with the extreme (or anomalous) rainfall episodes from 1998 to 2015, which are defined as the top 5% daily rainfall amounts among those occurring during the study period. The daily mean flow fields used for the spectral analysis are calculated as an arithmetic mean of the six-hourly reanalysis data set.

2.2. Spectral Analysis and Filtering

The spectral analysis and filtering algorithms used in this work follow those of Liu et al. (2014). They are performed with the fast Fourier transform (FFT) algorithm, which is useful for identifying prominent temporal

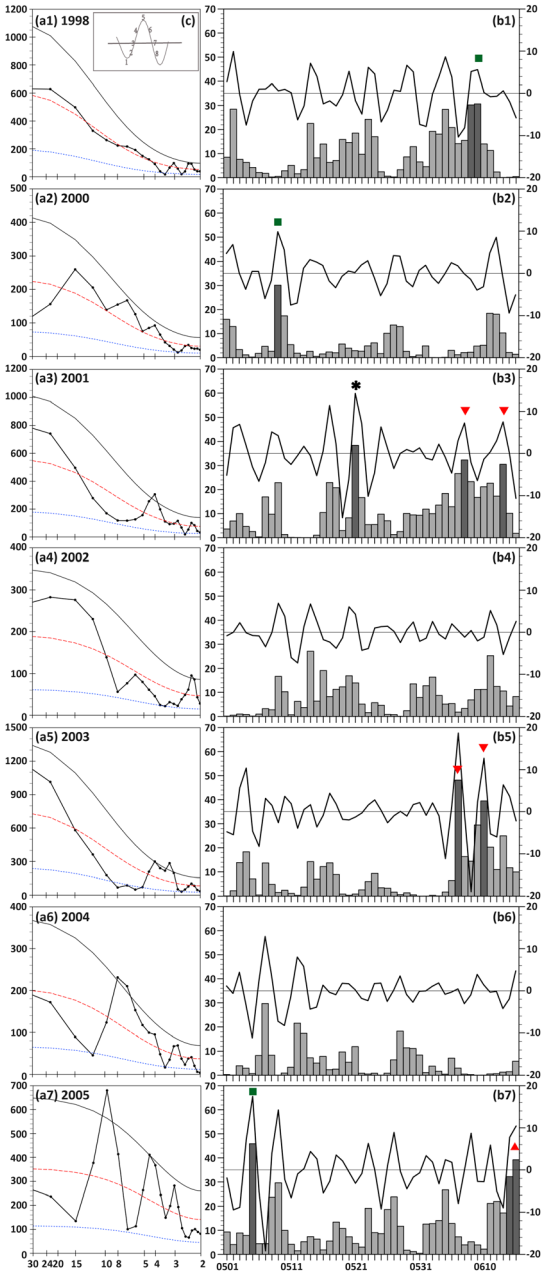

Figure 2a. (a) Power spectra of the CMORPH daily rainfall averaged in the key region (see the inner box in Figures 1a and 1c) during the period of 1 May to 15 June for years (1) 1998, (2) 2000, (3) 2001, (4) 2002, (5) 2003, (6) 2004, (7) 2005, (8) 2007, (9) 2008, (10) 2009, (11) 2010, (12) 2012, (13) 2013, and (14) 2015, showing the calculated spectrum (thick solid line with dots), Markov red-noise spectrum (red dashed lines), and 90% upper (thin solid lines) confidence bound. The abscissa has been rescaled to the natural logarithm of frequency. (b) As in (1)–(14) of (a) except for the time series of the domain-averaged daily rainfall (mm, bars), which is scaled on the left vertical axis, as well as the bandpass-filtered daily rainfall (mm) of 3–8 days in black (right vertical axis). Dark-gray bars indicate the extreme rainfall days within the top 5% intensity. Red lower/upper triangles, blue circle, green square, and black asterisk indicate the extreme rainfall episodes associated with the LTM type originated from the Tibetan Plateau/SCS, the UTM type, the trough type, and the anticyclone type, respectively. (c) Schematic diagram showing the eight phases in one life cycle used in the phase analysis.

ranges of rainfall fluctuations in any selected region. A 3–8 day filter is applied to extract signals associated with synoptic-scale disturbances. The statistical significance of their power spectra is tested using the method of Gilman et al. (1963).

An FFT analysis of the CMORPH daily rainfall and ERA-Interim daily mean circulation data sets is carried out for the presummer rainy seasons of 1998 to 2015. A phase analysis of the daily rainfall rates is performed to identify the spatial structures and temporal evolution of individual disturbances. Similarly, the filtered horizontal wind vectors obtained using the ERA-Interim data are utilized to identify atmospheric synoptic-scale disturbances. Anomalies of vertical velocity, relative vorticity, divergence, and equivalent potential temperature obtained from the ERA-Interim data are used to investigate the relevant dynamic and thermodynamic processes associated with the synoptic-scale disturbances.

3. Overview

In this section, we present the domain-averaged rainfall from 1 April to 30 June during 1998–2015 and discuss the spatial characteristics of the domain-averaged rainfall from the associated climatology. A synoptic-scale frequency mode associated with major extreme daily rainfall episodes is identified using the spectral analysis and filtering algorithms. The synoptic-scale disturbances associated with the identified extreme rainfall episodes are categorized into three types according to the dominant anomalies that contribute to each extreme rainfall episode.

3.1. The Daily Precipitation Series

As Luo et al. (2017), the south China region of interest (hereafter referred to as the key region) covers an area of 110°E–117°E, 20°N–25°N (see Figure 1). It consists of the provinces of Guangdong (GD) and Guangxi (GX) and part of the northern SCS. This area is located to the south of the Nanling Mountains, with scattered orography in the coastal areas of GD (Figure 1a). It is evident from Figure 1b that the domain-averaged daily rainfall within the key region is much less in April than in May and June and that heavier rainfall occurs from the middle of May to the middle of June. However, there are some landfalling typhoons or tropical cyclones over south China after 15 June (e.g., 23 June 2015) that would "contaminate" the spectral analysis of anomaly fields associated with extreme-rain-producing MCSs over the continental regions. Hence, the time period of 1 May to 15 June is chosen for this study, which is consistent with the presummer rainy season discussed in Luo et al. (2017). Note that the following results in section 4 are insensitive to the time windows if the period of 15 April to 15 June is used. Distribution of the 18 year averaged accumulative precipitation during 1 May 1 to 15 June, given in Figure 1c, shows maximum rainfall centers in central GD, eastern GX, and the southern coastal region of GD. These centers are mostly located within the key region, into which a moist tongue extends from the southwest (Figure 1d). On the other hand, in order to further eliminate the impact of landfalling typhoons on the relationship between extreme rainfall and anomalous frequency modes, the years with the typhoon impact during the abovementioned study period have also been excluded for this study. They are year 1999 (Typhoon Meggie, 6–8 June), year 2006 (Typhoon Chanchu, 17–18 May), year 2011 (Typhoon Sarika, 10–11 June), and year 2014 (Typhoon Magibis, 15–17 June).

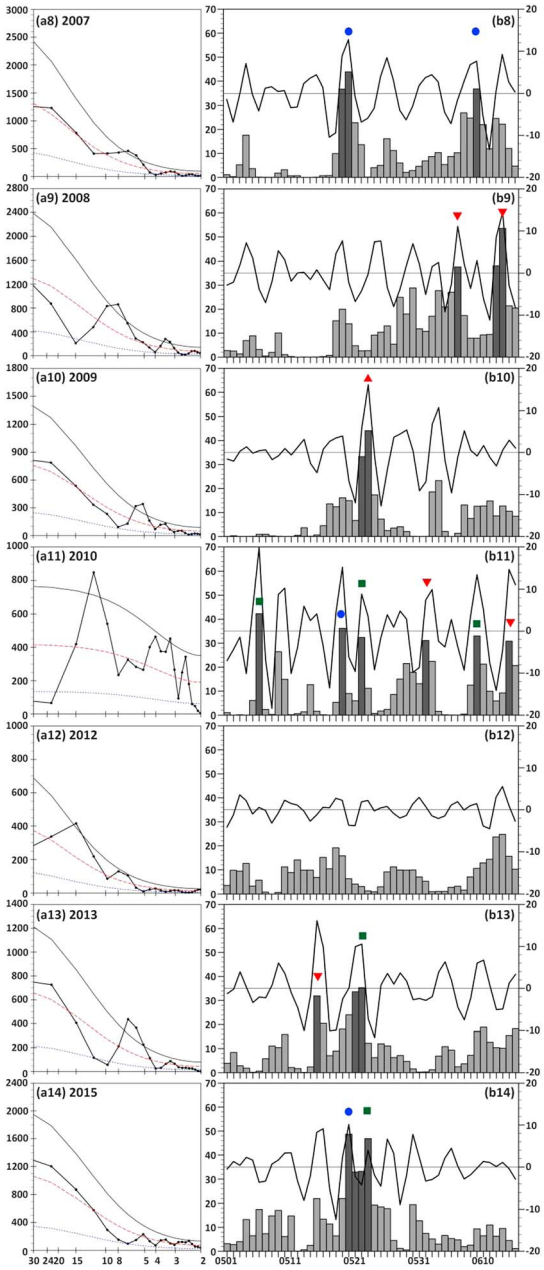

Figure 2b.

3.2. Selection of Extreme Rainfall Episodes

To help understand the influence of synoptic-scale disturbances on the generation of anomalous daily rainfall over south China, the power spectra of the domain-averaged daily rainfall rates for each of the 14 years are presented in Figures 2a1–2a14, together with Markov's red-noise spectrum and the 90% upper confidence bound. Obviously, the frequency bands on days 3–8 (i.e., synoptic timescale) are pronounced against the red-noise background and the 90% upper confidence bound for most years, with a significant correlation coefficient (0.55) between the domain-averaged daily rainfall and the bandpass-filtered rainfall (not shown). These results indicate that extreme rainfall production in south China is closely related to synoptic-scale disturbances during the presummer rainy season.

To obtain a better view of the characteristics of major extreme rainfall episodes, we have selected 32 extreme rainfall days whose daily rainfall rates are in the top 5% of all rainfall days during the study period (see dark-gray bars in Figures 2b1–2b14). The domain-averaged rainfall amount of these extreme rainfall days all exceed 30 mm/day. The top 5% of daily rainfall rates are consistent with the wettest phase of the bandpass-filtered precipitation at the synoptic scale (Figures 2b1–2b14). The wettest phase is identified from a life cycle of eight phases in Figure 2c (given as an inset in Figure 2a1), with the driest phase as phase 1 and the wettest phase as phase 5 corresponding to the minimal and maximal rainfall amounts, respectively. For the purpose of examining how the synoptic-scale disturbances influence positively the development of extreme rainfall events, only phases 1–5 are examined in this study. As some of the top 5% of extreme rainfall days last continuously within one life cycle (Figures 2b and 2c), they are considered as one rainfall episode, giving 24 extreme rainfall episodes (indicated by triangles in Figures 2b1–2b14) after the bandbass-filtered circulation analysis is performed.

The contribution of the synoptic disturbance to the overall unfiltered anomalies is calculated following the work of Liu et al. (2014) and Li and Zhou (2015). Based on the anomaly and filtered rainfall variances, the synoptic-scale mode contributes about 50%–61% from phases 1 to 5 for the selected extreme rainfall episodes. The percentages are smaller for the moisture flux convergence in phases 1 and 5 (25%, 31%), but up to 68% in phase 3 (Table 2). Altogether, this periodic phenomenon can explain a significant part of the episodic events.

3.3. Classification of Bandpass-Filtered Circulations

To fully investigate the impact of 3–8 day bandpass-filtered circulation on the extreme rainfall episodes over south China, we examine the filtered anomalous circulations associated with each extreme rainfall episode identified in the preceding subsection. The daily 3–8 day bandpass-filtered circulations are obtained against the daily total circulation of the corresponding years. Results show that all of the extreme rainfall episodes are associated with either cyclonic or anticyclonic anomalies in the wettest phase. Based on their three-dimensional anomaly structures and the distance of their lower-level (850 hPa) circulation centers from south China in the wettest phase, they are categorized into three types, as given in Table 1. That is, when a lower-level cyclonic anomaly in the wettest phase directly influences a rainfall episode in south China, that is, the distance between the cyclonic circulation center and the south China region is within 500 km, this episode is categorized into a "cyclone" type (Figures 3a and 3b) to be examined in section 4.1. There are 15 episodes of the cyclone type, which account for 62.5% of all the extreme rainfall episodes. The cyclone-type episodes are further divided into the "lower tropospheric migratory" and "upper tropospheric migratory" subgroups, hereafter referred to

Table 1
Summary Chart of the Classified Three Categories of Extreme Rainfall Episodes

Category name (# of episodes; %)			Date (yyyymmdd)
Cyclone (15; 62.5%)	Lower-tropospheric migratory (11; 73.3%)	Tibetan Plateau originated (9; 81.8%)	20010607, 20010613, 20030606, 20030610, 20080606, 20080613, 20100601, 20100614, 20130515
		South China Sea originated (2; 18.2%)	20050615, 20090523
	Upper-tropospheric migratory (4; 26.7%)		20070520, 20070609, 20100519, 20150520
Trough (8; 33.3%)			19980609, 20000509, 20050505, 20100506, 20100522, 20100609, 20130522, 20150523
Anticyclone (1; 4.2%)			20010521

as "LTM" and "UTM," respectively, depending on what level their anomalous vorticity has peaked. In the LTM episodes, a closed cyclonic anomaly could be clearly observed in the lower troposphere originating either around Sichuan basin downstream of the Tibetan Plateau (9) or over the SCS (2) during at least one phase prior to the wettest phase, while in the UTM episodes, a closed cyclonic anomaly could be seen in the upper troposphere starting from phase 1, with a closed cyclonic anomaly only emerging in the wettest phase over south China in the lower troposphere. When a cyclonic anomaly, centered in north China with a distance of $>$500 km, affects the extreme rainfall in the south China through its southwestward-extended deep trough anomaly, this rainfall episode is regarded as a "trough" type to be examined in section 4.2. Eight episodes of the trough type are found, accounting for 33.3% of all the episodes. Among the 24 extreme rainfall episodes of interest, only one episode is associated with a lower-level anticyclonic anomaly over the key region, which is categorized into an "anticyclone" type. Of notice are the analogous structures of bandpass-filtered circulation at 700 hPa and 850 hPa (not shown). Therefore, only the bandpass-filtered circulations at 850 hPa will be used in the remaining paper.

After grouping the same type of circulation anomalies, a composite analysis, which is a simple and effective way to identify and classify synoptic-scale circulation patterns, is performed to examine their relationship with various extreme rainfall episodes. Due to the consistency between the phase of bandpass-filtered rainfall and the days of total rainfall amounts, it is common to match phase 1 as day -2 and phase 3 as day -1, given that phase 5 matches the wettest day as day 0. Then, we can obtain their composites of each type phase by phase in the bandpass-filtered anomaly fields and day by day in the total fields. The Student t test was performed to show the significance of the composite field. The composite results of the horizontal maps and vertical cross sections are examined in the next section to show how the structure and evolution of different types of synoptic disturbances evolve to influence extreme rainfall production over south China.

4. Results

4.1. Relationship Between Filtered Circulations of Cyclone Type and Extreme Rainfall Episodes

The cyclone type of anomalies, consisting of the LTM and UTM subgroups, account for a major proportion of the selected extreme rainfall episodes (Table 1). The lower-level cyclonic anomalies of LTM episodes are mostly found to originate from the southeastern edge of the Tibetan Plateau, accompanied by a cold front,

Table 2
The Standard Deviation of the Anomalies of Domain-Averaged Rainfall (mm day^{-1}) and Moisture Flux Convergence (850 hPa; 10^{-9} kg m^{-2} s^{-1}), Respectively, Over the South China on Phase 1, Phase 3, and Phase 5

	Unfiltered			Synoptic		
	P1	P3	P5	P1	P3	P5
Rainfall	9.32	12.35	6.92	5.13 (55%)	5.63 (50%)	4.24 (61%)
Moisture convergence	10.87	7.23	9.77	2.75 (25%)	4.91 (68%)	2.98 (31%)

Note. Values in parentheses denote the percentage contribution of the synoptic disturbance to the overall unfiltered anomalies. P1, P3, and P5 are short for phase 1, phase 3, and phase 5, respectively.

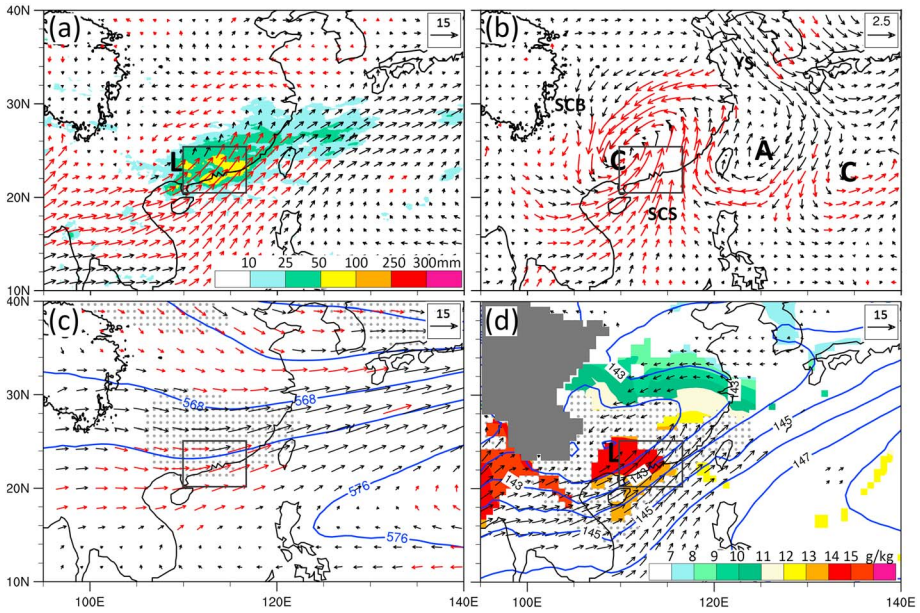

Figure 3. Composite fields for the LTM cyclone-type episodes, in which the low-level cyclonic anomalies originated from the southeastern edge of the Tibetan Plateau, in the peak phase. (a) The daily-mean rotational wind at 850 hPa and daily rainfall anomaly (mm; shading), (b) the 3–8 day bandpass-filtered daily-mean rotational wind (m s^{-1}) at 850 hPa, (c) the daily-mean wind and geopotential height (contoured in blue at 10 gpm; intervals) at 500 hPa, and (d) the daily-mean wind (m s^{-1}), specific humidity (g kg^{-1}; shadings), and geopotential height contoured in black (10 gpm) at 850 hPa. Letters "L," "A," and "C" denote a low pressure system, an anticyclonic anomaly, and a cyclonic anomaly, respectively. Symbols "SCB," "SCS," and "YS" in (b) denote the location of the Sichuan Basin, the South China Sea, and the Yellow Sea, respectively. Black contours at the left-upper corner of (a)–(c) denote the distribution of 3,000 m terrain elevation, and black lines denote the coastal lines. Gray shading coverage in (d) implies the area underneath the terrain. The red vectors in (a)–(c), the gray dots in (c) and (d), and the vectors and shadings in (d) denote the values that are over the 90% confidence level.

and then move southeastward to south China during the wettest phase, while the lower-level cyclonic anomalies of the UTM episodes emerge locally over south China during the wettest phase. It is therefore of interest to examine how differently the two types of anomalies evolve to influence the generation of extreme rainfall over south China. Moreover, the lower-level cyclonic anomalies in two extreme episodes of the LTM type have originated from the SCS. It is worth examining how the cyclonic anomaly of these two episodes influence the generation of extreme rainfall over south China and how they are different from the cyclonic anomalies that originated from the Tibetan Plateau.

4.1.1. The LTM Cyclone Type

A composite analysis of the total and bandpass-filtered fields associated with the LTM cyclone type of episodes shows the presence of a low-pressure system and a collocated cyclonic anomaly across the western boundary of south China (Figures 3a, 3b, and 3d), giving rise to a warm and moist tongue generated by southwesterly winds from the Indian Ocean and SCS into the key region (Figures 3b and 3d). Of relevance is that the extreme rainfall occurs along the southwesterly wind regions with abundant moisture. At 500 hPa, we see the distribution of a trough, albeit relatively weak, over south China that provides favorable quasi-geostrophic forcing and a dominant anticyclonic circulation associated with the west Pacific subtropical high (WPSH) with its ridge axis located at 16–17°N. Clearly, the WPSH plays an important role in maintaining a southwesterly flow through the key region (Figure 3c), thus enhancing water vapor convergence in the key region and providing a favorable environment for the occurrence of extreme rainfall over south China (Wang & Gu, 2016).

After seeing the composite relationship between the LTM cyclone-type of extreme rainfall episode and its synoptic flow pattern, it is useful to examine how it is related to the filtered synoptic-scale disturbances in different phases. For this purpose, Figure 4 presents the corresponding phase relationship in both the lower (850 hPa) and upper troposphere (200 hPa) in phases 1 (minimum), 3 (null), and 5 (peak; Figure 2c). It is evident that south China is dominated by a northerly wind anomaly associated with an anticyclonic circulation, denoted by "A," in the lower troposphere in phase 1, which results in a large

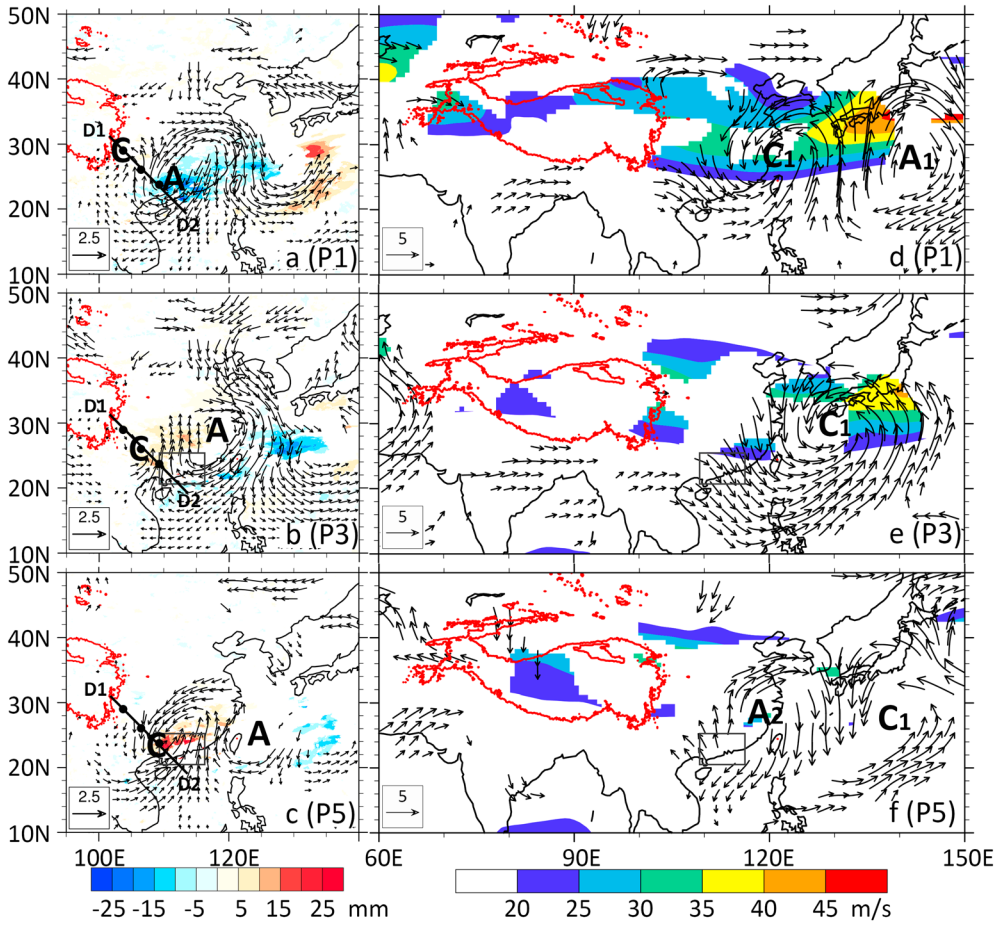

Figure 4. Composite 3–8 day bandpass-filtered fields at phases 1, 3, and 5 (P1, P3, and P5) for the LTM cyclone-type episodes, in which the low-level cyclonic anomalies originated from the southeastern edge of the Tibetan Plateau. (a)–(c) The daily-mean rotational wind (m s^{-1}) at 850 hPa and daily rainfall (mm). (d)–(f) The daily-mean rotational wind (m s^{-1}) and corresponding total wind speed (shadings, m s^{-1}) at 200 hPa. Letters "A" and "C" denote the centers of an anticyclonic anomaly and a cyclonic anomaly, respectively. Dots in (a)–(c) are the centers of the cyclonic anomaly at each phase. Thick black lines in (a)–(c) represent the paths of the cyclonic anomaly, and the cross sections in Figure 5 are taken. Red contours indicate the 3,000 m terrain elevation. Shadings and vectors denote anomalies that are over the 90% confidence level.

negative rainfall anomaly (Figure 4a). Meanwhile, a cyclonic disturbance, denoted by "C," is present to the northwest of south China, and then it moves southeastward as the anticyclonic anomaly moves toward the northeast (Figure 4b). The cyclonic disturbance moves southeastward into the key region in phase 5 when the associated southwesterly anomaly transports warm, moist air from the SCS (Figure 4c). It is worth noting that south China is located in the entrance region of the upper-level jet stream in a Rossby wave train in phase 5 (Figure 4f). The corresponding upward motion, though weak, would at least provide a favorable condition for lifting the warm, moist air transported from the SCS. However, this eastward-propagating upper-level Rossby wave train does not appear to determine the southeastward propagation of the cyclonic anomaly, because of their different source regions: midlatitude westerlies for the former but the Tibetan Plateau for the latter.

Vertical cross sections through the cyclonic anomaly track from phase 1 to phase 3 and phase 5 are given in Figure 5, following closely those of Jiang et al. (2004), Abhik et al. (2013), and Wang and Duan (2015), in order to demonstrate the structures and evolution of vertical anomalous circulations in relation to the extreme rainfall production during the different rainfall development stages. In phase 1, little rainfall develops because south China is in the descending branch with upper- (lower-) level northwesterly converging (southerly divergent) anomalous flows (cf. Figures 5a, 5b, 4a, and 4d). A lower-tropospheric positive vorticity anomaly (i.e., associated with "C" in Figure 4a), peaked at 850 hPa, is collocated with an organized upward motion with

a more pronounced convergence in the lowest 150 hPa in the northwestern portion of the anomaly (Figure 5b). Of importance is the vertical northwestward tilt of the upward motion, suggesting the presence of baroclinicity, that is, a cold front that originates or enters from the southeast side of the Tibetan Plateau. Correspondingly, a negative (positive) equivalent potential temperature (θ_e) anomaly dominates south China (the upward motion region to the northwest), as shown in Figure 5c.

In phase 3, the anomalous southerly ascending motion begins to dominate south China (cf. Figures 4b and 5d–5f). In particular, the ascending motion becomes more upright compared to that in phase 1 (cf. Figures 4a and 4d), indicating the presence of significant latent heat release in the midtroposphere. The previous-mentioned frontal character is still evident, as suggested by the northwestward tilt of the vorticity and divergence structures in the lower troposphere. This shows that the southeastward movement of the lower-level cyclonic anomaly is closely related to the cold front that becomes shallower and less distinct as it propagates southward. Clearly, it is the warm and moist southwesterly air ascending over the southeastward propagating frontal surface that plays an important role in preconditioning a favorable environment for the subsequent generation of extreme rainfall over south China.

After reaching the wettest phase 5 (cf. Figures 4c and 5g–5i), a more upright vertical motion (i.e., driven by latent heat release) dominates south China, especially near the center of the cyclonic anomaly. Its depth also increases, as indicated by the peak divergence level, for example, from 250 hPa in phases 1 and 3 to 175 hPa in phase 5. Of importance is that the cyclonic anomaly at the center (i.e., denoted by dashed lines), increasing in intensity over time, is shifted downward from 700 hPa in phase 1 to approximately 800 hPa in phase 3 and about 900 hPa in phase 5 (cf. Figures 5a, 5d, and 5g). This is indicative of the spin-up of the cyclonic anomaly as a result of a positive feedback process established between the lower-level convergence, upward motion, latent heat release, and surface pressure fall. As the lower-level convergence is enhanced, it will help strengthen the upward motion, increase the latent heat release, and lead to a surface pressure fall, which in turn will enhance the lower-level convergence. This positive feedback will facilitate the generation of extreme rainfall, given the continuous supply of warm and moist air in the south-to-southwesterly flow. Indeed, a deep layer of positive θ_e anomalies appears in the upward motion region and even in the upper-level downward motion regions during this wettest phase (Figure 5i).

For comparison, the evolution of the cyclonic anomaly that originated from the SCS is shown in Figure 6. Unlike the interaction between the upper level and lower level observed in the LTM type originating from the Tibetan Plateau, this type only shows significant lower-level features (Figure 6), which leads to a relatively weak convergence. The cyclonic anomaly originating from the SCS in phase 1 produced significant positive rainfall anomaly over SCS (Figure 6a). This cyclonic anomaly is enhanced in phase 3, as it moved toward south China (Figure 6b), along the edge of the WPSH (not shown). In the wettest phase, the cyclonic anomaly reached south China, causing extreme rainfall in that region (Figure 6c). Note that a northeasterly dominated the northern south China in phase 5 (Figure 6c), which is different from the strong southwesterly transporting warm and moist air from the SCS in the LTM type that originated from the Tibetan Plateau (Figure 4c). Hence, the main difference of these two types of LTM episodes in the wettest phase would be the moisture content within south China and the strength of the cyclonic anomaly.

4.1.2. The UTM Cyclone Type

The UTM cyclone-type episodes produce extreme rainfall mainly located over the offshore areas near the GD coasts and the central GD province (Figure 7a). Compared to the LTM cyclone-type episodes, this type of episode shows a weaker low-pressure center in the overall field (cf. Figures 3d and 7d) and a less organized anomalous cyclonic circulation in the 3–8 day bandpass-filtered wind field (cf. Figures 3b and 7b). Of major difference from the LTM type is the generation of a cyclonic anomaly with a northeasterly flow instead of a southwesterly flow influencing south China (cf. Figures 7b and 3b). Moreover, the 500 hPa trough and the WPSH over south China are weaker and stronger, respectively, than those associated with the LTM cyclone-type episode, albeit having similar circulation patterns (cf. Figures 3c, 3d, 7c, and 7d).

Note that the lower-level cyclonic anomaly contributing to the UTM cyclone-type extreme rainfall episodes does not appear until the wettest phase. Specifically, in phase 1, an intense traveling cyclonic anomaly "C" is centered in north China (near 38°N, 120°E), with positive rainfall anomalies in central and southwest China where anomalous northwesterly flows converge with anomalous southwesterly flows (Figure 8a). In this phase, south China is influenced more by a deep anticyclonic anomaly with negative vorticity

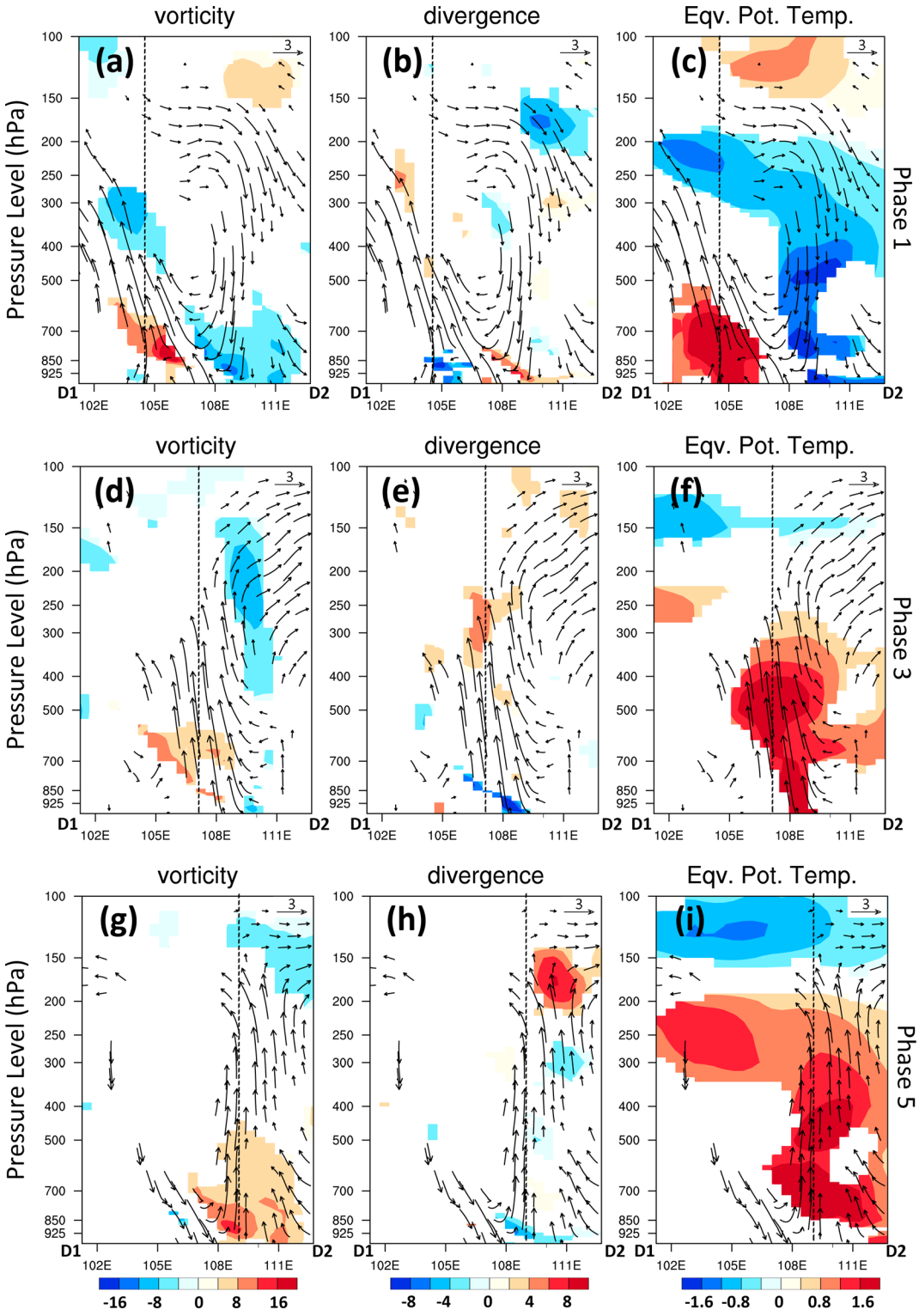

Figure 5. Composite cross section of 3–8 day bandpass-filtered fields of the LTM cyclone episodes, in which the low-level cyclonic anomalies originated from the southeastern edge of the Tibetan Plateau, at (a)–(c) phase 1, (d–f) phase 3, and (g–i) phase 5 for (a, d, g) vorticity (10^{-6} s^{-1}), (b, e, h) divergence (10^{-6} s^{-1}), and (c, f, i) equivalent potential temperature (K) anomaly. The vectors are the meridional component (m/s) and vertical component (10 cm/s). The dash lines at each phase indicate the location of the cyclonic anomaly at the corresponding phases. Location of the cross sections is indicated by the northwest-southeast oriented black line in Figures 4a–4c. Shadings and vectors denote anomalies that are over the 90% confidence level.

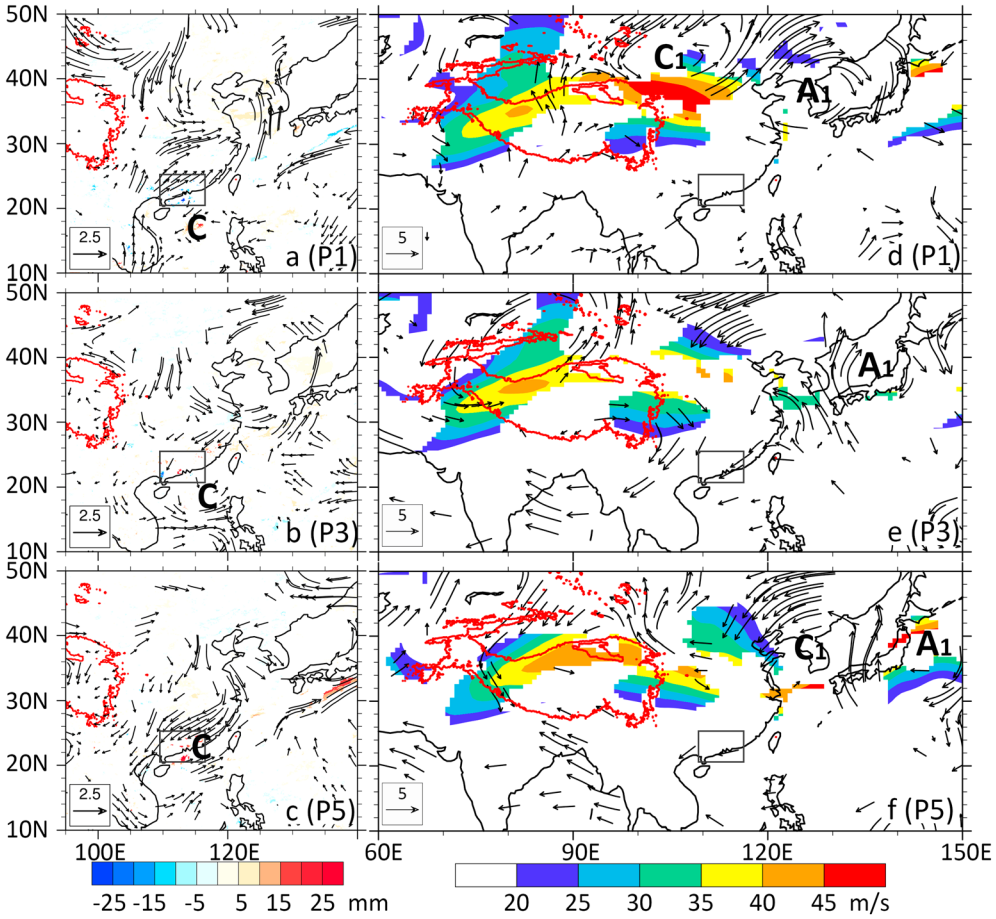

Figure 6. As in Figure 4 except that the low-level cyclonic anomalies originated from the SCS. The vectors and shadings are the anomalies over the 80% confidence level.

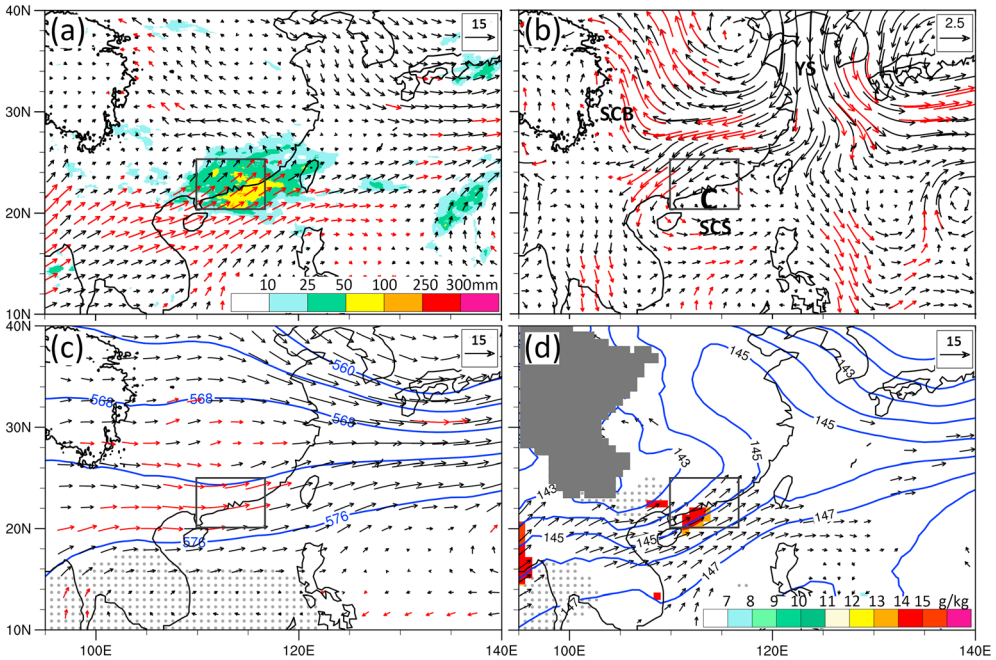

Figure 7. As in Figure 3 but for the UTM-type episodes.

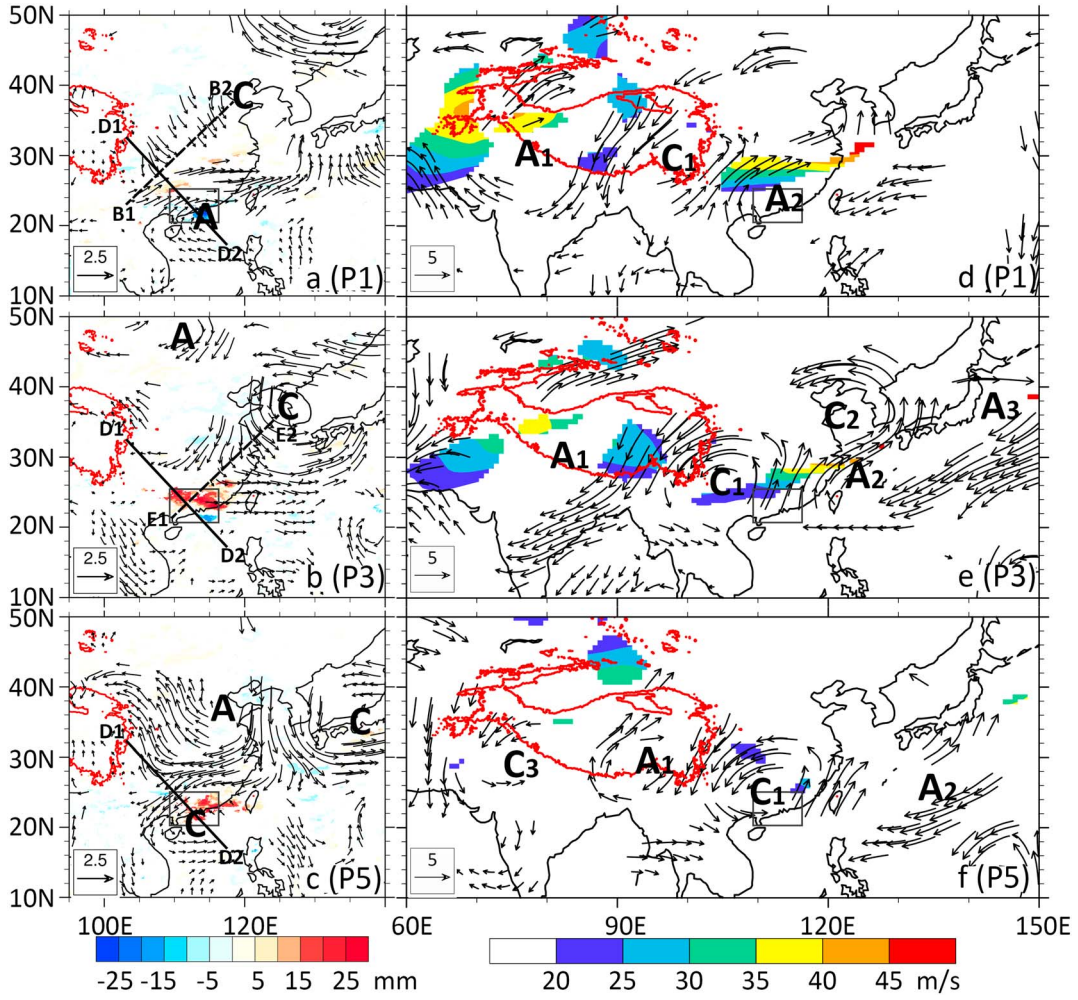

Figure 8. As in Figure 4 but for the UTM-type episodes. The dash lines indicate the location of the trough.

(Figures 8a, 8b, and 9a), a negative θ_e anomaly, and descending motion (Figure 9c). A southeastward moving cold front, collocated with the trough axis, is evident (cf. Figures 8a–8c, 9c, 9f, and 9i). All these suggest that the larger-scale conditions ahead of the frontal zone in phase 1 are unfavorable for rainfall production in south China.

In phase 3, as the intense cyclonic anomaly "C" moves to South Korea and extends up to 200 hPa (Figures 8b and 8e), west-to-southwesterly flows associated with its southwestward-extending deep trough begin to influence south China, producing a west-east-oriented belt of positive rainfall anomalies along the northern border of the key region. Associated with the low-level trough is an intense cyclonic anomaly "C_1" in the anticyclonic entrance region of an upper-level jet stream (Figures 8b and 8e). Note that "C_1" coincides with a positive θ_e anomaly (or a warm anomaly due to the presence of little moisture) above 200 hPa and mass convergence (and descending motion) in/below the northeasterly flows between "C_1" and "A_1" (cf. Figures 8e and 9f). This upper-level warm anomaly appears to account for the formation of a cyclonic anomaly (or lower pressure) in the upper troposphere (cf. Figures 9c, 9f, 9i and 9a, 9d, 9g). In contrast, the low-level to midlevel cyclonic anomalies in phase 3 are clearly attributed to latent heat release associated with the positive rainfall anomalies along the northern border of the key region, as indicated by a deep layer of intense upward motion (cf. Figures 9d, 9e, and 8b).

Like the LTM-type episode, a closed lower-level cyclonic anomaly with increased cyclonic vorticity also appears in phase 5, which is mainly a result of latent heat release in convective storms occurring ahead of the cold front (Figures 8c and 9g). This cyclonic anomaly is much weaker in intensity and smaller in size than the northwestward-tilted, upper-level counterpart. Unlike those associated with the LTM-type episode, the ascending motion and positive θ_e anomalies over the key region are much shallower and less organized,

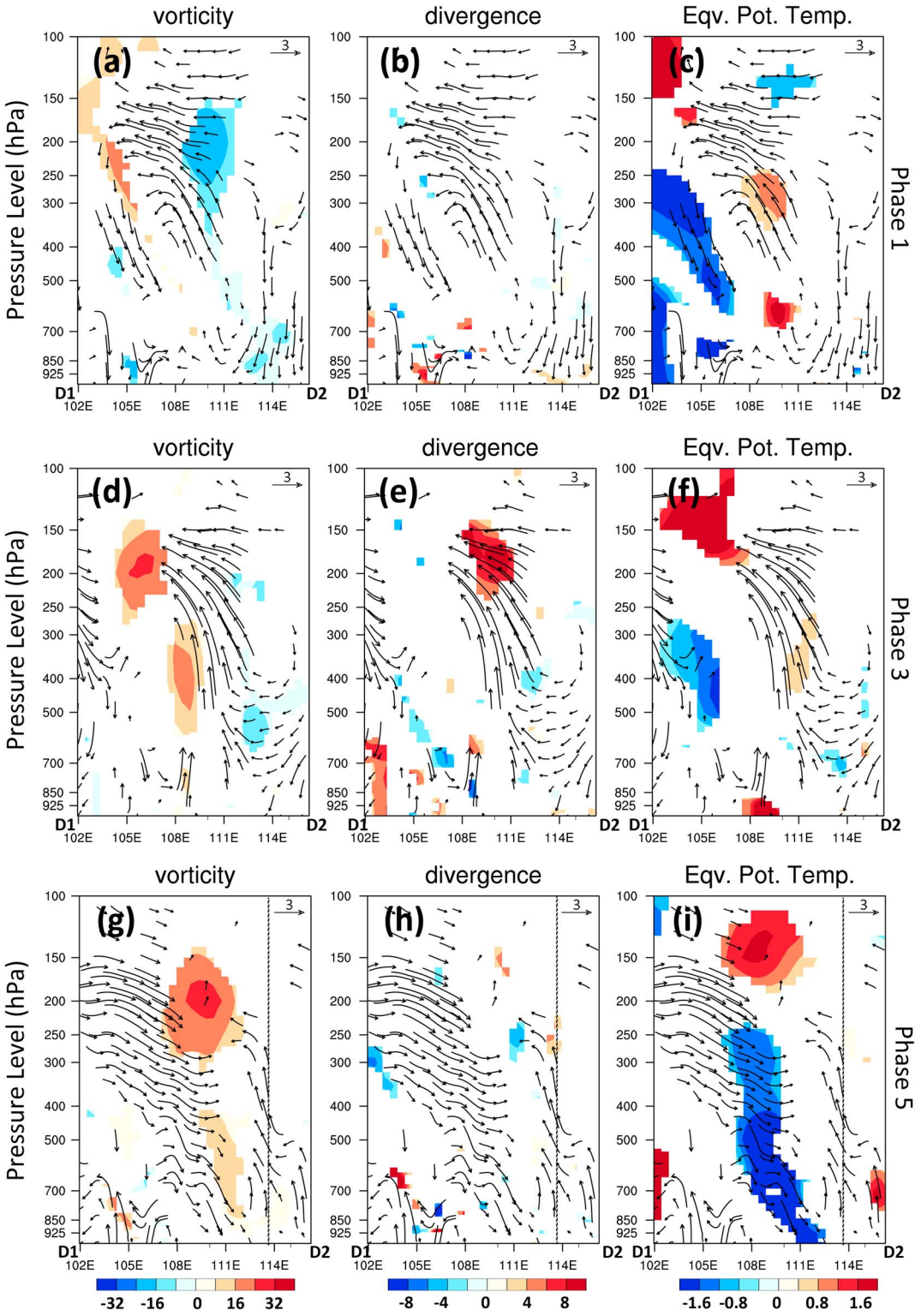

Figure 9. As in Figure 5 but for the UTM-type episodes along lines D1–D2 in Figures 8a–8c. The dashed lines at phase 5 indicate the location of the cyclonic anomaly at phase 5.

but the opposite is true for the descending motion and negative θ_e anomalies behind the cold front (cf. Figures 9i and 6i). Despite the presence of the weaker cyclonic anomaly, its associated rainfall amount is comparable to that of the LTM type (Figure 2; cf. Figures 3a and 7a).

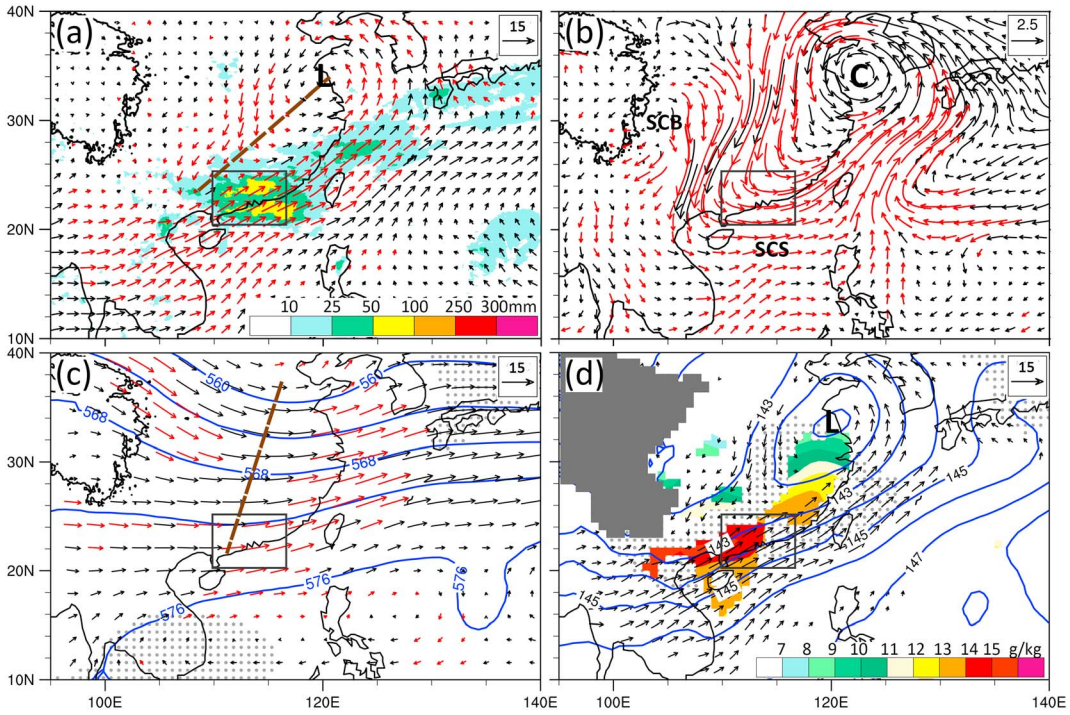

Figure 10. As in Figure 3 but for the trough-type episodes.

Note that it is the anomalous latent heat release in the extreme-rainfall producing MCSs that contributes mostly to the generation of lower-level cyclonic anomaly during the wettest phase in the UTM-type episode. However, the intense upper-level cyclonic anomaly is always observed during all phases in the UTM-type episode, whereas the LTM-type episode only exhibits the lower-level cyclonic anomaly. Thus, this appears to distinguish the UTM- from LTM-type episodes in terms of their origin and evolution.

4.2. Relationship Between Filtered Circulations of Trough Type and Extreme Rainfall Episodes

In the trough-type episode, south China is situated ahead of a low-level trough axis associated with an extratropical cyclone centered on the western Yellow Sea, as also indicated by the anomaly fields (Figures 10a and 10b). They are in significant contrast to the cyclone-type episodes, in which a major cyclone is located on the west of the key region (Figures 3d and 7d). Like the cyclone type, a moist tongue in the southwesterly flow at 850 hPa and a trough at 500 hPa, respectively, provide favorable moisture supply and quasi-geostrophic forcing for the extreme rainfall production over south China (Figures 10c and 10d).

In this type of episode, south China experiences the passage of an anomalous ridge in phase 1, followed by an anomalous trough in phase 3 (Figures 11a and 11b). An elongated rainfall belt begins to appear in the north of the key region where a southwesterly flow converges with a northwesterly flow. This anomalous rainfall belt shifts with the trough into the key region in phase 5. Note that like the previously discussed disturbances, the cyclonic anomaly centered on the western Yellow Sea at this wettest phase could also be traced back to the east side of the Tibetan Plateau (Figures 11a–11c), as part of a Rossby wave train in the middle and upper troposphere. It is evident from Figures 11d–11f that the key region is always located in the right entrance region of an upper-level jet stream, and in particular, phase 5 coincides with divergent south to southeasterly outflows aloft, which plays an important role in generating a favorable secondary circulation (Figure 12).

Similar to the UTM-type episode, the trough-type episode also experiences the passage of a surface cold front moving toward south China, together with a midlevel trough, in the wettest phase (Figure 12c). A well-developed secondary circulation is observed, with an ascending branch in the warm and moist sector ahead of the front, and a descending branch in the cold and dry region behind (Figure 12c), which appears to be a common vertical circulation associated with extreme rainfall production over south China, based on the results presented herein. Nevertheless, the substantial difference between the trough type and the UTM

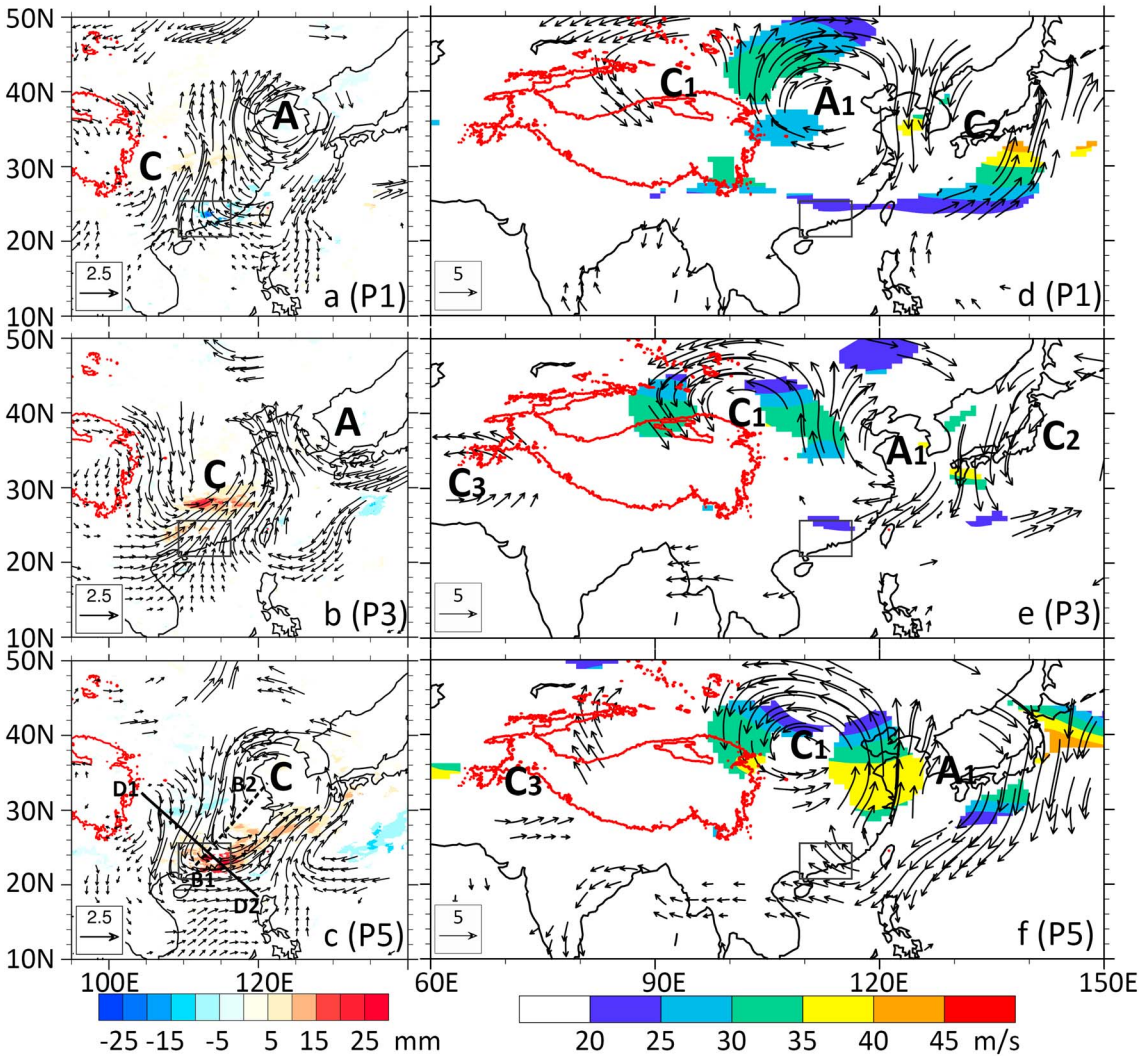

Figure 11. As in Figure 4 but for the trough-type episodes.

type occurs in the wettest phase when the extreme rainfall arrives, which is how we categorize these three types of episodes. A strong trough anomaly reaches south China in phase 3 of the UTM episode and dissipates in phase 5, while it reaches south China in the wettest phase in the trough-type episode directly influencing the extreme rainfall production. Hence, the trough is one phase behind in the trough-type episode than that in the UTM type. Therefore, what distinguishes the UTM-type and the trough-type episodes would be the main anomaly that contributed to the extreme rainfall.

4.3. Relationship Between Filtered Circulations of Anticyclonic Type and Extreme Rainfall Episodes

The extreme rainfall episode associated with the anticyclone-type circulation is primarily influenced by the strong southwesterly at lower levels (Figures 13a–13c). South China is located between the couplet of cyclonic and anticyclonic anomalies in phase 1, which leads to strong negative rainfall anomaly due to the less favorable environment such as the water vapor transportation and the instability. The cyclonic anomaly dissipates in phase 3, while the anticyclonic anomaly occupies south China, resulting in a strong wind and water vapor flux divergence over south China (not shown). This anticyclonic anomaly continues to move eastward and is located near the east of south China in phase 5, with the associated southwesterly transporting warm and moist air to south China. Also noted is that south China is located at the upper-level jet entrance in a Rossby wave train during this phase. The upward motion, though weak, still provides a favorable condition for lifting the warm, moist air from the SCS.

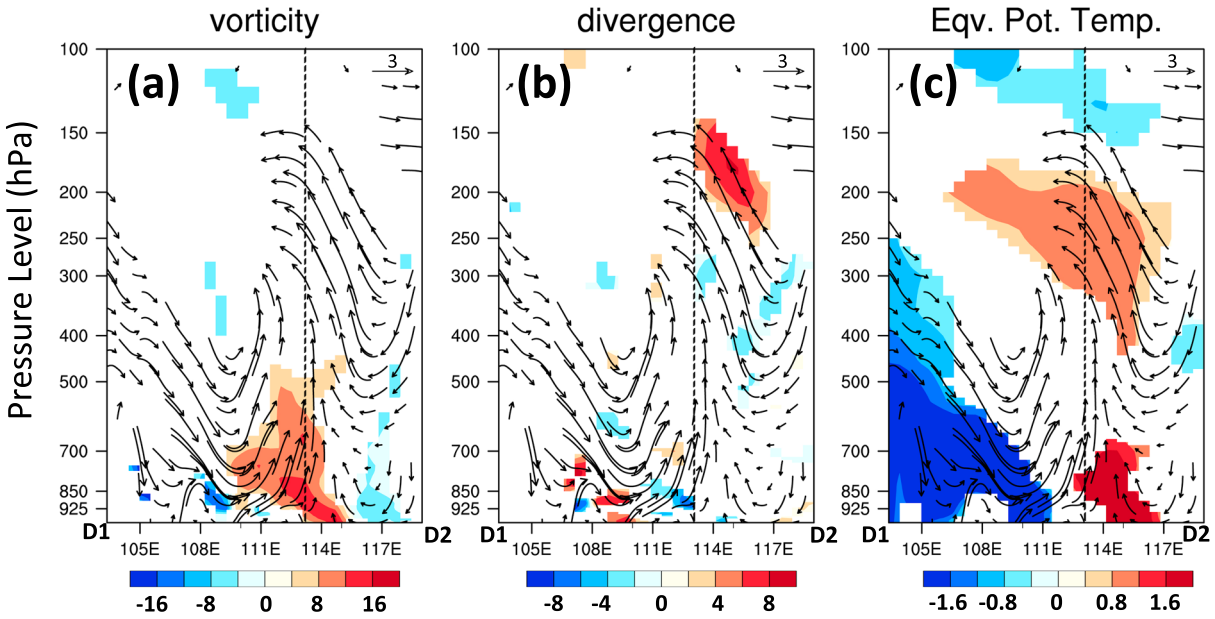

Figure 12. As in Figure 5 but for the trough-type episodes at phase 5 along lines D1-D2 in Figure 11c. The dashed lines at each phase indicate the location of the crossover point of B1-B2 and D1-D2 at phases 5.

5. Summary and Discussion

In this study, we investigate the origin and evolution of synoptic disturbances related to the development of the presummer (1 May to 15 June) extreme rainfall over south China between 1998 and 2015 (excluding 1999, 2006, 2011, and 2014) through analyzing bandpass-filtered anomalous circulations. Twenty-four extreme-rainfall episodes with the top 5% daily rainfall amount are found, and the synoptic disturbances influencing their generations are categorized into three types of episodes, that is, cyclonic, trough, and anticyclonic types, according to their three-dimensional anomaly structures and the distance of their circulation centers from south China during the wettest phase. Results show that the three types consist of 15, 8, and 1 extreme rainfall episodes, respectively, and demonstrate that the first two types of anomaly mostly originate near the southeastern side of the Tibetan Plateau, except for two episodes of the cyclonic type originating from the SCS. The cyclone-type episodes are composed of two subgroups of migratory cyclonic anomalies: one always in the lower troposphere (LTM) with little evidence of cyclonic anomalies in the upper troposphere during all phases and the other always in the upper troposphere (UTM) during all phases, but with a closed cyclonic anomaly in the lower troposphere only during the wettest phase. The single anticyclonic-type episodes are also briefly examined in this study.

An analysis of the composite fields shows that the LTM-type episode originating from the Tibetan Plateau is closely related to a southeastward-moving cold front, with continuous high-θ_e supply in the south-to-southwesterly flows after entering the wettest phase over south China. The lower-level cyclonic/anticyclonic couplet moves eastward to influence south China under the westerly influences, with the cyclonic anomaly enhanced by latent heat release, given abundant moisture in the south and southwesterlies from the SCS and Indian Ocean. On the other hand, the LTM-type originating from the SCS has less moisture to transport due to the dominant northeasterly over northern south China during the wettest phase compared with those from the Tibetan Plateau. The extreme rainfall production of the UTM type is closely related to the southeastward propagation of a strong upper-level cyclonic anomaly that favors quasi-geostrophically the lower-level upward motion and hence enhances the lower-level convergence. The resulting latent heat release further strengthens the upward motion and boundary layer convergence, assisting in the generation of a lower-level cyclonic anomaly. The trough type of extreme rainfall episode is associated with a trough extending southwestward from a traveling cyclonic anomaly located in north China during the wettest phase. This cyclonic anomaly appears to be part of a midlatitude Rossby wave train in the middle and upper troposphere. When the trough reaches south China, the associated lower-level vorticity is strengthened by strong latent heat release during the wettest phase. The single extreme rainfall episode associated with the anticyclonic anomaly is influenced by strong water vapor flux in its northwest periphery, which causes a large positive rainfall anomaly over inland south China.

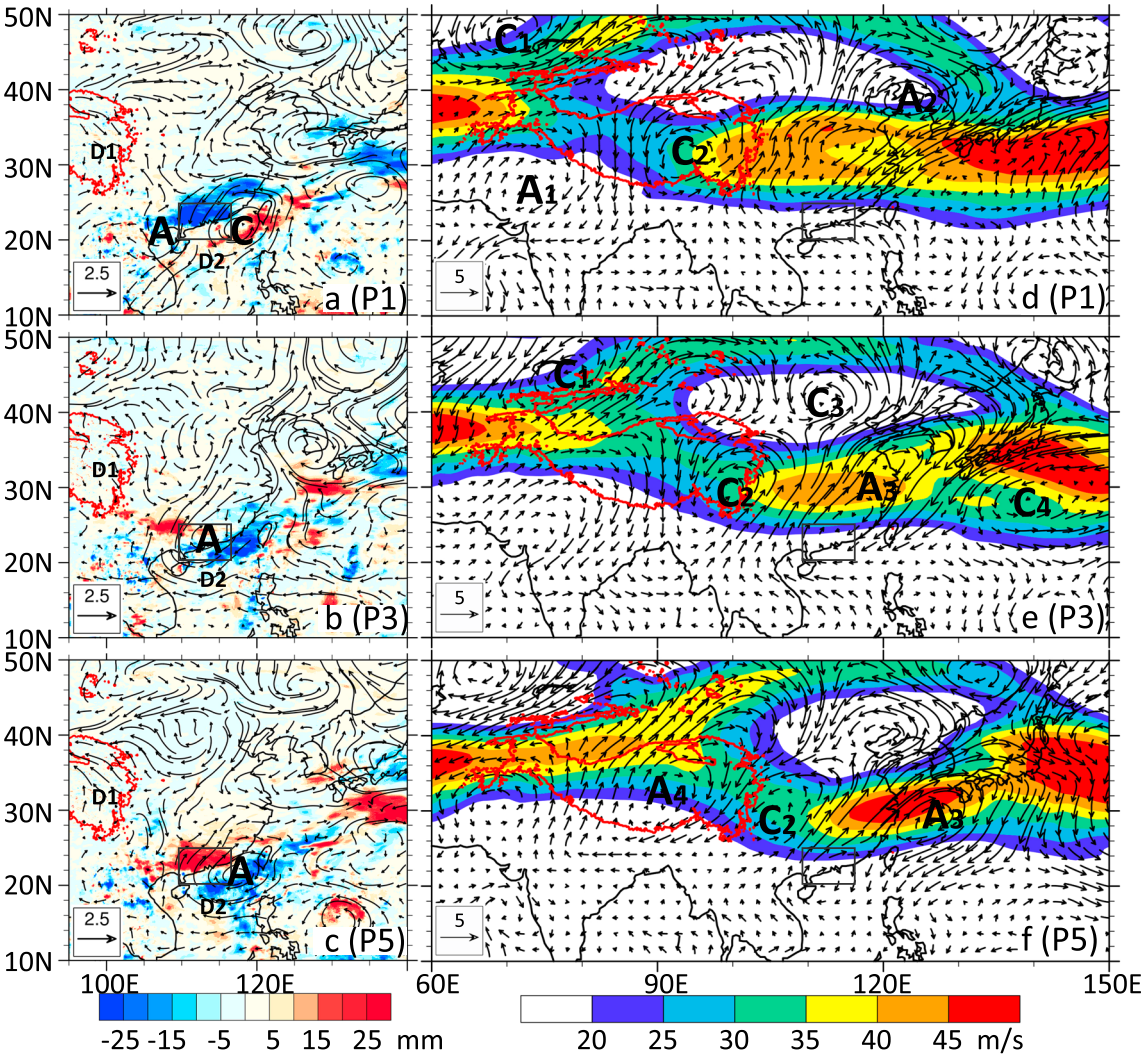

Figure 13. As in Figure 4 but for the anticyclone-type episodes. The field is not the composite result; thus, no significant test was conducted.

In conclusion, the presummer extreme rainfall episodes over south China are significantly influenced by synoptic distances that originate at the southeastern side of the Tibetan Plateau with their peak intensities in the lower or upper troposphere, or extend from north China, accompanied by a southeastward-moving surface cold front or a Rossby wave train in the middle and upper troposphere. Abundant moisture supply in the low-level south-to-southwesterly flows from the SCS and Indian Ocean around the East Asian monsoon onset appears to play an important role in generating extreme rainfall and enhancing cyclonic anomalies over south China. The results have significant implications for the understanding of the relationship between the presummer extreme rainfall episodes in south China and synoptic-scale disturbances that originate at the downstream side of the Tibetan Plateau or in north China. Compared with previous studies that discussed the impact of the synoptic disturbances and intraseasonal oscillation on heavy rainfall either in a single case (e.g., Liu et al., 2014) or in a long-term composition (e.g., Li & Zhou, 2015), this work provides a comprehensive study of the production of extreme rainfall over south China in a climatological scenario, by categorizing different types of synoptic disturbances of relevance and then compositing each type. Such categorization and composition of the extreme rainfall episodes, which is still limited in the literature, separate various factors that could possibly contribute to the rainfall, thus providing useful information in forecasting extreme rainfall. Nevertheless, further studies are needed to gain deeper insight into how the high-frequency disturbances interact with atmospheric intraseasonal variations in contributing to extreme rainfall in south China during the presummer rainy season.

Acknowledgments
We wish to thank Hongbo Liu of the Institute of Atmospheric Physics, Chinese Academy of Sciences (IAP) and Jisong Sun of the Chinese Academy of Meteorological Sciences (CAMS) for providing constructive suggestions, and Wen Zhou and Richard Li for providing useful information about the calculation of the contribution of the synoptic disturbance. This work was funded by the National Natural Science Foundation of China (91437104, 41775050), the China Postdoctoral Science Foundation (2016 M601197), the Public Welfare Scientific Research Projects in Meteorology (GYHY201406013), and the Basic Research and Operation Funding of the CAMS (2017Z006). The ERA data were downloaded from http://apps.ecmwf.int/datasets, and the CMORPH data were downloaded from ftp://ftp.cpc.ncep.noaa.gov/precip/global_CMORPH/. The typhoon information was obtained from http://agora.ex.nii.ac.jp/digital-typhoon/index.html.en.

References

Abhik, S., Halder, M., Mukhopadhyay, P., Jiang, X., & Goswami, B. N. (2013). A possible new mechanism for northward propagation of boreal summer intraseasonal oscillations based on TRMM and MERRA reanalysis. *Climate Dynamics*, *40*(7-8), 1611–1624. https://doi.org/10.1007/s00382-012-1425-x

Berry, G. J., Reeder, M. J., & Jakob, C. (2012). Coherent synoptic disturbances in the Australian monsoon. *Journal of Climate*, *25*(24), 8409–8421. https://doi.org/10.1175/JCLI-D-12-00143.1

Chang, C.-P., Harr, P. A., & Chen, H. J. (2005). Synoptic disturbances over the equatorial South China Sea and western maritime continent during boreal winter. *Monthly Weather Review*, *133*, 489–503.

Chang, C.-P., Hou, S.-C., Kuo, H.-S., & Chen, G. T.-J. (1998). The development of an intense East Asian summer monsoon disturbance with strong vertical coupling. *Monthly Weather Review*, *126*(10), 2692–2712. https://doi.org/10.1175/1520-0493(1998)126%3C2692:TDOAIE%3E2.0.CO;2

Chen, G. J., Wei, F. Y., & Xiu, X. J. (2014). Intraseasonal oscillation of South China Sea summer monsoon and its influence on regionally persistent heavy rainfall over southern China. *Journal of Meteorological Research*, *28*(2), 213–229.

Chen, G. T. J. (1983). Observational aspects of the Mei-Yu phenomena in subtropical China. *Journal of the Meteorological Society of Japan*, *61*(2), 306–312. https://doi.org/10.2151/jmsj1965.61.2_306

Chen, G. T.-J., Wang, C.-C., & Lin, D. T.-W. (2005). Characteristics of low-level jets over northern Taiwan in Mei-Yu season and their relationship to heavy rain events. *Monthly Weather Review*, *133*(1), 20–43. https://doi.org/10.1175/MWR-2813.1

Chen, G. T.-J., Wang, C.-C., & Lin, L.-F. (2006). A diagnostic study of a retreating Mei-Yu front and the accompanying low-level jet formation and intensification. *Monthly Weather Review*, *134*(3), 874–896. https://doi.org/10.1175/MWR3099.1

Chen, G. T.-J., & Yu, C.-C. (1988). Study of low-level jet and extremely heavy rainfall over northern Taiwan in the Mei-Yu season. *Monthly Weather Review*, *116*(4), 884–891. https://doi.org/10.1175/1520-0493(1988)116%3C0884:SOLLJA%3E2.0.CO;2

Chen, Y., & Zhai, P. (2014). Two types of typical circulation pattern for persistent extreme precipitation in central–eastern China. *Quarterly Journal of the Royal Meteorological Society*, *140*(682), 1467–1478. https://doi.org/10.1002/qj.2231

Dee, D. P., Uppala, S. M., Simmons, A. J., Berrisford, P. P., Poli, P., Kobayashi, S., et al. (2011). The ERA-Interim reanalysis: Configuration and performance of the data assimilation system. *Quarterly Journal of the Royal Meteorological Society*, *137*(656), 553–597. https://doi.org/10.1002/qj.828

Ding, Y. (1994). *Monsoons over China* (419 pp.). Dordrecht, Netherlands: Kluwer Academic.

Doswell, C. A., Brooks, H. E., & Maddox, R. A. (1996). Flash flood forecasting: An ingredients based methodology. *Weather and Forecasting*, *11*(4), 560–581. https://doi.org/10.1175/1520-0434(1996)011%3C0560:FFFAIB%3E2.0.CO;2

Fitzjarrald, D. R., Sakai, R. K., Moraes, O. L. L., Cosme de Oliveira, R., Acevedo, O. C., Czikowsky, M. J., & Beldini, T. (2008). Spatial and temporal rainfall variability near the Amazon-Tapajo's confluence. *Journal of Geophysical Research*, *113*, G00B11. https://doi.org/10.1029/2007JG000596

Fu, S. M., Zhao, S., Sun, J., & Li, W. (2010). One kind of vortex causing heavy rainfall during pre-rainy season in south China (in Chinese with English abstract). *Chinese Journal of Atmospheric Sciences*, *34*, 235–252.

Gilman, D. L., Fuglister, F. J., & Mitchell Jr, J. M. (1963). On the power spectrum of "red noise". *Journal of the Atmospheric Sciences*, *20*(2), 182–184. https://doi.org/10.1175/1520-0469(1963)020%3C0182:OTPSON%3E2.0.CO;2

Gu, G., & Zhang, C. (2001). A spectrum analysis of synoptic-scale disturbances in the ITCZ. *Journal of Climate*, *14*(12), 2725–2739. https://doi.org/10.1175/1520-0442(2001)014%3C2725:ASAOSS%3E2.0.CO;2

Hirpa, F. A., Gebremichael, M., & Hopson, T. (2010). Evaluation of high-resolution satellite precipitation products over very complex terrain in Ethiopia. *Journal of Applied Meteorology and Climatology*, *49*(5), 1044–1051. https://doi.org/10.1175/2009JAMC2298.1

Hong, W., & Ren, X. J. (2013). Persistent heavy rainfall over south China during May-August: Subseasonal anomalies of circulation and sea surface temperature. *Acta Meteorologica Sinica*, *27*(6), 769–787. https://doi.org/10.1007/s13351-013-0607-8

Huang, L., & Luo, Y. (2017). Evaluation of quantitative precipitation forecast by TIGGE ensembles for south China during the presummer rainy season. *Journal of Geophysical Research: Atmospheres*, *122*, 8494–8516. https://doi.org/10.1002/2017JD026512

Huang, L., & Meng, Z. (2014). Quality of the target area for metrics with different nonlinearities in a mesoscale convective system. *Monthly Weather Review*, *142*(7), 2379–2397. https://doi.org/10.1175/MWR-D-13-00244.1

Jiang, X. A., Li, T., & Wang, B. (2004). Structures and mechanisms of the northward propagating boreal summer intraseasonal oscillation. *Journal of Climate*, *17*, 1022–1039.

Jiao, M., Yao, X., Zhou, B., & Yang, K. (2004). *Synoptic analysis of summer 2003 heavy rainfall over Huai River basin* (in Chinese) (215 pp.). Beijing: China Meteorological Press.

Johns, R. H., & Doswell, C. A. (1992). Severe local storms forecasting. *Weather and Forecasting*, *7*(4), 588–612. https://doi.org/10.1175/1520-0434(1992)007%3C0588:SLSF%3E2.0.CO;2

Joyce, R. J., Janowiak, J. E., Arkin, P. A., & Xie, P. (2004). CMORPH: A method that produces global precipitation estimates from passive microwave and infrared data at high spatial and temporal resolution. *Journal of Hydrometeorology*, *5*(3), 487–503. https://doi.org/10.1175/1525-7541(2004)005%3C0487:CAMTPG%3E2.0.CO;2

Kummerow, C., Barnes, W., Kozu, T., Shiue, J., & Simpson, J. (1998). The Tropical Rainfall Measuring Mission (TRMM) sensor package. *Journal of Atmospheric and Oceanic Technology*, *15*(3), 809–817. https://doi.org/10.1175/1520-0426(1998)015%3C0809:TTRMMT%3E2.0.CO;2

Li, C. Y., & Zhou, W. (2015). Multiscale control of summertime persistent heavy precipitation events over south China in association with synoptic, intraseasonal, and low frequency background. *Climate Dynamics*, *45*(3-4), 1043–1057. https://doi.org/10.1007/s00382-014-2347-6

Liu, H., Zhang, D.-L., & Wang, B. (2008). Daily to submonthly weather and climate characteristics of the summer 1998 extreme rainfall over the Yangtze River basin. *Journal of Geophysical Research*, *113*, D22101. https://doi.org/10.1029/2008JD010072

Liu, H. B., Yang, J., Zhang, D.-L., & Wang, B. (2014). Roles of synoptic to quasi-biweekly disturbances in generating the summer 2003 heavy rainfall in East China. *Monthly Weather Review*, *142*(2), 886–904. https://doi.org/10.1175/MWR-D-13-00055.1

Luo, Y., Wang, H., Zhang, R., Qian, W., & Luo, Z. (2013). Comparison of rainfall characteristics and convective properties of monsoon precipitation systems over south China and the Yangtze and Huai river basin. *Journal of Climate*, *26*(1), 110–132. https://doi.org/10.1175/JCLI-D-12-00100.1

Luo, Y., Zhang, R., Wan, Q., Wang, B., Wong, W. K., Hu, Z., et al. (2017). The Southern China Monsoon Rainfall Experiment (SCMREX). *Bulletin of the American Meteorological Society*, *98*(5), 999–1013. https://doi.org/10.1175/BAMS-D-15-00235.1

Luo, Y. L., Qian, W. M., Zhang, R. H., & Zhang, D.-L. (2013). Gridded hourly precipitation from high-density rain gauge network over the Yangtze-Huai Rivers basin during the 2007 Mei-yu season and comparison with CMORPH. *Journal of Hydrometeorology*, *14*(4), 1243–1258. https://doi.org/10.1175/JHM-D-12-0133.1

Mao, J., & Wu, G. (2006). Intraseasonal variations of the Yangtze rainfall and its related atmospheric circulation features during the 1991 summer. *Climate Dynamics*, *27*(7-8), 815–830. https://doi.org/10.1007/s00382-006-0164-2

Mao, J., Zhang, S., & Wu, G. (2010). 20–50-day oscillation of summer Yangtze rainfall in response to intraseasonal variations in the subtropical high over the western North Pacific and South China Sea. *Climate Dynamics*, *34*(5), 747–761. https://doi.org/10.1007/s00382-009-0628-2

Ninomiya, K., & Akiyama, T. (1992). Multi-scale features of Baiu, the summer monsoon over Japan and East Asia. *Journal of the Meteorological Society of Japan*, *70*(1B), 467–495. https://doi.org/10.2151/jmsj1965.70.1B_467

Pan, W. J., Mao, J. Y., & Wu, G. X. (2013). Characteristics and mechanism of the 10–20-day oscillation of spring rainfall over southern China. *Journal of Climate*, *26*(14), 5072–5087. https://doi.org/10.1175/JCLI-D-12-00618.1

Pereira Filho, A. J., Carbone, R. E., Janowiak, J. E., Arkin, P., Joyce, R., Hallak, R., & Ramos, C. G. M. (2010). Satellite rainfall estimates over South America—Possible applicability to the water management of large watersheds. *Journal of the American Water Resources Association*, *46*(2), 344–360. https://doi.org/10.1111/j.1752-1688.2009.00406.x

Qian, J. H., Tao, W. K., & Lau, K. M. (2004). Mechanisms for torrential rain associated with the Mei-Yu development during SCSMEX 1998. *Monthly Weather Review*, *132*, 2–27.

Shen, Y., Xiong, A., Wang, Y., & Xie, P. (2010). Performance of high-resolution satellite precipitation products over China. *Journal of Geophysical Research*, *115*, D02114. https://doi.org/10.1029/2009JD012097

Sun, X. G., Jiang, G. X., Ren, X. J., & Yang, X. Q. (2016). Roles of intraseasonal oscillation in the persistent extreme precipitation over the Yangtze River basin during June 1998. *Journal of Geophysical Research: Atmospheres*, *121*, 10,453–10,469.

Tam, C. Y., & Li, T. (2006). The origin and dispersion characteristics of the observed tropical summertime synoptic-scale waves over the western Pacific. *Monthly Weather Review*, *134*(6), 1630–1646. https://doi.org/10.1175/MWR3147.1

Tao, S., & Ding, Y. (1981). Observational evidence of the influence of the Qinghai-Xizang (Tibet) Plateau on the occurrence of heavy rain and severe convective storms in China. *Bulletin of the American Meteorological Society*, *62*(1), 23–30. https://doi.org/10.1175/1520-0477(1981)062%3C0023:OEOTIO%3E2.0.CO;2

Wang, C.-C., Hsu, J. C.-S., Chen, G., Chen, G. T.-J., & Lee, D.-I. (2014). A study of two propagating heavy-rainfall episodes near Taiwan during SoWMEX/TiMREX IOP-8 in June 2008. Part I: Synoptic evolution, episode propagation, and model control simulation. *Monthly Weather Review*, *142*, 2619–2643.

Wang, H., Luo, Y., & Jou, B. (2014). Initiation, maintenance, and properties of convection in an extreme rainfall event during SCMREX: Observational analysis. *Journal of Geophysical Research: Atmospheres*, *119*, 13,206–13,232. https://doi.org/10.1002/2014JD022339

Wang, L., & Gu, W. (2016). The eastern China flood of June 2015 and its causes. *Scientific Bulletin*, *61*, 178–184.

Wang, M. R., & Duan, A. M. (2015). Quasi-biweekly oscillation over the Tibetan Plateau and its link with the Asian summer monsoon. *Journal of Climate*, *28*(12), 4921–4940. https://doi.org/10.1175/JCLI-D-14-00658.1

Wu, M. W., & Luo, Y. L. (2016). Mesoscale observational analysis of lifting mechanism of a warm-sector convective system producing the maximal daily precipitation in China mainland during pre-summer rainy season of 2015. *Journal of Meteorological Research*, *30*(5), 719–736. https://doi.org/10.1007/s13351-016-6089-8

Xia, R., Zhang, D.-L., & Wang, B. (2015). A 6-yr cloud-to-ground lightning climatology and its relationship to rainfall over central and eastern China. *Journal of Applied Meteorology and Climatology*, *54*(12), 2443–2460. https://doi.org/10.1175/JAMC-D-15-0029.1

Yang, H., & Li, C. (2003). The relation between atmospheric intraseasonal oscillation and summer severe flood and drought in the Changjiang–Huaihe River basin. *Advances in Atmospheric Sciences*, *20*, 540–553.

Yang, J., Bao, Q., Wang, B., Gong, D.-Y., He, H., & Gao, M.-N. (2013). Distinct quasi-biweekly features of the subtropical East Asian monsoon during early and late summers. *Climate Dynamics*, *42*(5-6), 1469–1486. https://doi.org/10.1007/s00382-013-1728-6

Yang, J., Wang, B., Wang, B., & Bao, Q. (2010). Biweekly and 21–30-day variabilities of the subtropical East Asian monsoon over the lower reach of Yangtze River basin. *Journal of Climate*, *23*(5), 1146–1159. https://doi.org/10.1175/2009JCLI3005.1

Zhang, M., & Zhang, D. L. (2012). Subkilometer simulation of a torrential-rain-producing mesoscale convective system in East China, part I: Model verification and convective organization. *Monthly Weather Review*, *140*(1), 184–201. https://doi.org/10.1175/MWR-D-11-00029.1

Zhang, Q., Tao, S., & Zhang, S. (2003). The persistent heavy rainfall over the Yangtze River valley and its associations with the circulations over East Asian during summer (in Chinese). *Chinese Journal of Atmospheric Sciences*, *27*, 1018–1030.

Zhang, X., Guo, P., & He, J. (2002). Characteristics of low frequency oscillation of precipitation and wind field in the middle and low reaches of the Yangtze River in summer 1991 (in Chinese). *Journal of Nanjing Institute of Meteorology*, *25*, 388–394.

Zhu, C., Nakazawa, T., Li, J., & Chen, L. (2003). The 30–60 day intraseasonal oscillation over the western North Pacific Ocean and its impacts on summer flooding in China during 1998. *Geophysical Research Letters*, *30*(18), 1952. https://doi.org/10.1029/2003GL017817